Photoreduction of SERS-Active Metallic Nanostructures on Chemically Patterned Ferroelectric Crystals

N. Craig Carville,[†,‡] Michele Manzo,[§] Signe Damm,[†] Marion Castiella,[‡,⊥] Liam Collins,[†,‡] Denise Denning,[†,‡] Stefan A. L. Weber,[‡] Katia Gallo,[§] James H. Rice,[†] and Brian J. Rodriguez[†,‡,*]

[†]School of Physics and [‡]Conway Institute of Biomolecular and Biomedical Research, University College Dublin, Belfield, Dublin 4, Ireland and [§]Department of Applied Physics, KTH-Royal Institute of Technology, Roslagstullbacken 21, 106 91 Stockholm, Sweden. [⊥]Present address: Institut National des Sciences Appliquées, 135 Avenue de Rangueil, 31400 Toulouse, France.

ABSTRACT

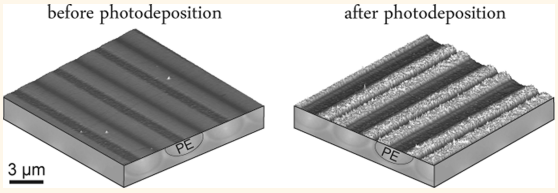

Photodeposition of metallic nanostructures onto ferroelectric surfaces is typically based on patterning local surface reactivity *via* electric field poling. Here, we demonstrate metal deposition onto substrates which have been chemically patterned *via* proton exchange (*i.e.*, without polarization reversal). The chemical patterning provides the ability to tailor the electrostatic fields near the surface of lithium niobate crystals, and these engineered fields are used to fabricate metallic nanostructures. The effect of the proton exchange process on the piezoelectric and electrostatic properties of the surface is characterized using voltage-modulated atomic force microscopy techniques, which, combined with modeling of the electric fields at the surface of the crystal, reveal that the deposition occurs preferentially along the boundary between ferroelectric and proton-exchanged regions. The metallic nanostructures have been further functionalized with a target probe molecule, 4-aminothiophenol, from which surface-enhanced Raman scattering (SERS) signal is detected, demonstrating the suitability of chemically patterned ferroelectrics as SERS-active templates.

KEYWORDS: ferroelectric · lithium niobate · proton exchange · nanofabrication · lithography · directed assembly · domain patterning · photochemistry · atomic force microscopy · Raman scattering

The polarization-mediated chemistry of ferroelectric surfaces could enable a new set of applications based on assembly of molecules and complex nanostructures and on local control of reactivity.[1,2] Recent efforts have explored polarization-dependent molecular absorption[3,4] and desorption,[5,6] ice nucleation,[7] and artificial photosynthesis.[8] One area that has attracted significant attention in the past decade is the photochemical reduction of metal nanoparticles, that is, photodeposition. Originally, this was demonstrated on barium titanate, whereby aqueous Ag^+ was reduced to metallic Ag^0 on the surface of positive domains.[9,10] Photochemical growth of metals on other ferroelectrics including lead zirconate titanate[11−15] and $LiNbO_3$ (lithium niobate (LN))[16−18] has been studied extensively. Photodeposition behavior has been found to depend on polarization effects (*e.g.*, bound polarization charge, screening charge, band bending) and defects and doping. Furthermore, depending on the illumination conditions (wavelength, intensity, illumination time, *etc.*), photoreduction can occur on both positively and negatively poled domains. Uniquely, for periodically poled LN crystals, photochemical reduction can result in the formation of nanowires that form along the domain wall.[19]

When a LN crystal is illuminated with a light source of energy higher than the band gap (~3.9 eV), electron−hole pairs are generated by optical absorption (the UV absorption edge is ~318 nm).[20] In the presence of the electrostatic field present at domain boundaries, these charges are spatially separated, forming space charge regions in the LN crystal. At the surface, these charge carriers can take part in reduction and oxidation reactions. In periodically poled LN, the photoreduction has been found to occur along 180° domain boundaries, resulting in the deposition of Ag at domain walls.[19] Away from the boundaries, the in-plane component of the electric field perpendicular to the domain walls is reduced. Depending on the illumination conditions, the photogenerated electron cannot be used for photodeposition unless there are local electronic or topographic defects or band bending. Recently, the dependence of photodeposition on LN surfaces on light

* Address correspondence to brian.rodriguez@ucd.ie.

Received for review June 7, 2012 and accepted July 9, 2012.

Published online July 09, 2012
10.1021/nn3025145

wavelength and intensity and on the concentration of the $AgNO_3$ solution has been reported by Sun *et al.*[21,22]

Domain patterning results in regions of opposite polarization and in LN is typically performed *via* electric field poling.[23] An alternative approach for patterning the electric fields at the surface of LN crystals is based on chemical patterning. Proton exchange (PE) is a process consisting of the substitution of Li^+ ions with H^+ ions provided by an acid solution, which modifies the properties of the surface,[24] and allows the optical, ferroelectric, and piezoelectric properties of the crystal to be tailored.[25,26] The PE surface layer has H^+ protons embedded in the crystalline lattice, forming a $H_xLi_{1-x}NbO_3$ compound.[27,28] The disruption of the crystal lattice induces a change in the surface properties. In LN, the polarization arises from the contribution of Li and Nb ions displaced with respect to the oxygen planes. Thus, by reducing the concentration of Li through PE, the intrinsic polarization is reduced. By applying this chemical patterning method periodically (*i.e.*, through a mask), this process can be used to modulate the polarization, and hence the electrostatic fields, at the surface of the LN crystal.[25,26]

Given the importance of interfaces (*e.g.*, photoconducting domain walls[29]) and defects on the properties and reactivity of LN, and the demonstrated impact of built-in electric fields associated with PE on domain switching,[25,26] in this study, we have explored the role periodic PE (PPE) engineered interfaces have on the photochemistry of LN surfaces. Notably, the nanowires formed on periodically poled LN have been shown to be conducting,[30] and such high aspect ratio (nanometer widths with micrometer lengths)[19] functional nanowires could be of technological relevance in, for example, biosensors and surface-enhanced Raman scattering (SERS) applications.[31,32] The width of the deposited nanowires, however, is confined to the domain wall width, and the shape of domains that can be fabricated on LN is strongly tied to the crystallographic axes, whereas the PE process is not confined by poling geometries. In addition, chemical patterning *via* PE does not require the application of large DC biases needed for periodic poling. Thus, it is possible to effectively pattern surface reactivity without electric field poling, and the crystal is used mainly as a mechanical support. The introduction of a chemical patterning technique provides an additional degree of freedom in tailoring the shape (*i.e.*, the width and the geometries) of the metallic nanostructures that can be fabricated on the ferroelectric surfaces.

Thus, photodeposition on ferroelectric surfaces allows for the control (*via* electrical and chemical patterning and *via* deposition conditions) of the size, shape, and distribution of metallic nanostructures, which will enable new ways to pattern arrays of complex nanostructures and control local reactivity from nano- to microscales. In addition, such ferroelectric templates are reusable (the structures can be removed) and reconfigurable (the pattern can be rewritten).

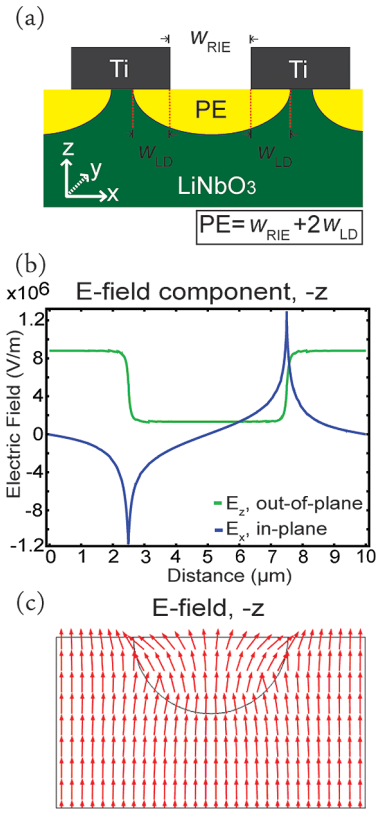

Figure 1. (a) Schematic diagram of the PPELN templates used. (b) Spatial distributions (over one PPELN period) of the in-plane (E_x) and out-of-plane (E_z) components of the electric field 10 nm below the $-z$ surface, and (c) vectorial electric field distributions around the PE region over a cross section (x, z) close to the $-z$ surface.

RESULTS

The fabrication of periodically proton-exchanged LN (PPELN) crystals is described in detail in the Materials and Methods section. Briefly, reactive ion etching (RIE) has been used to create openings in a Ti mask, and PE has been performed through these openings, leaving a PPELN crystal with LN and PE regions, as illustrated in Figure 1a. The lateral diffusion (LD) of protons underneath the Ti stripes[25,26] results in final PE widths which are broader than the original mask openings ($w_{PE} = w_{RIE} + 2\,w_{LD}$).

In order to visualize the electric fields near the surface of the PPELN samples, the out-of-plane (E_z) and in-plane (E_x) built-in electric field components were modeled using COMSOL Multiphysics, as shown in Figure 1b for the $-z$ crystal surface. At the boundary between the PE and LN regions, E_x is at a maximum. The electric field lines in the PPELN crystal are shown in Figure 1c for the $-z$ crystal surface. The fields are highly inhomogeneous across the PE–LN interfaces. It is expected that the electric field at these interfaces will

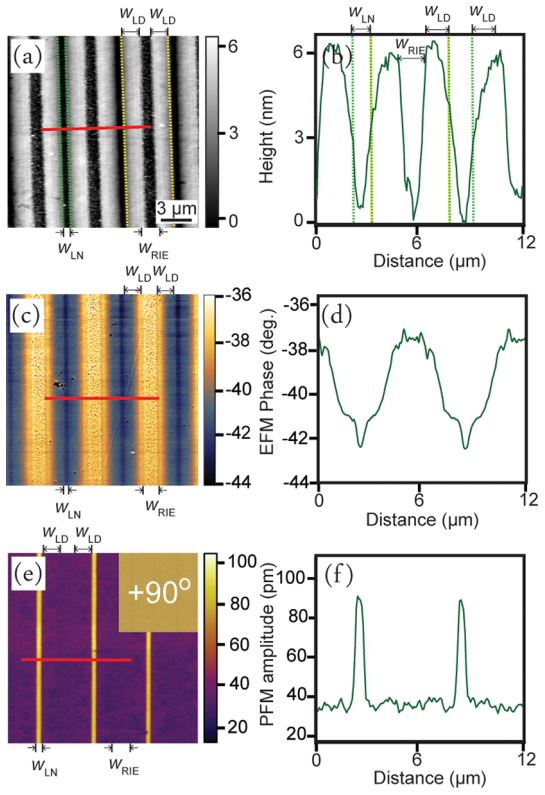

Figure 2. PPELN $-z$ surface prior to photodeposition. (a) AFM topography image and (b) corresponding line profile from the region indicated in (a). (c) EFM phase image and (d) corresponding line profile from the region indicated in (c). (e) PFM amplitude image with an inset of the PFM phase image with a scan area of 20 μm and a data scale of 360°, and (f) corresponding line profile from the region indicated in (e). The scale bar in (a) also applies to (c,e).

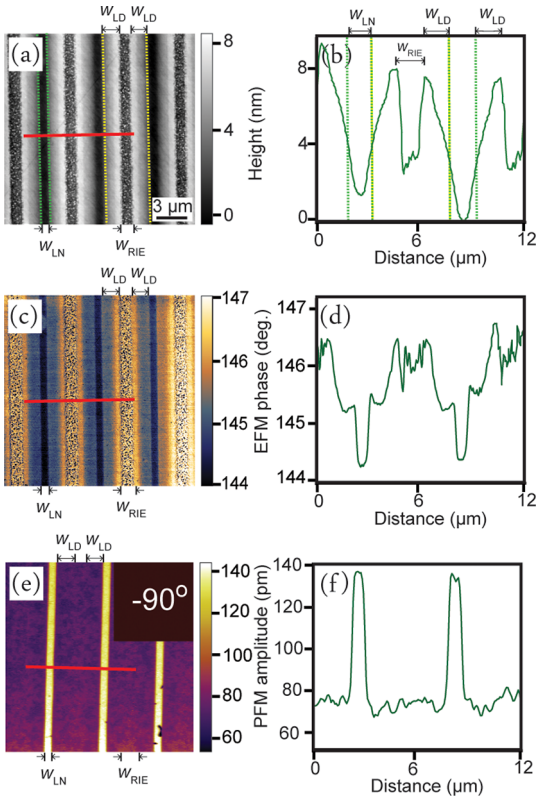

Figure 3. PPELN $+z$ surface prior to photodeposition. (a) AFM topography image and (b) corresponding line profile from the region indicated in (a). (c) EFM phase image and (d) corresponding line profile from the region indicated in (c). (e) PFM amplitude image with an inset of the PFM phase image with a scan area of 20 μm and a data scale of 360°, and (f) corresponding line profile from the region indicated in (e). The scale bar in (a) also applies to (c,e).

separate the photogenerated electron−hole pairs. The electric fields for the $+z$ crystal point in the opposite direction to those in Figure 1.

Prior to processing, the LN crystals, which have been polished to an optical grade, have a surface roughness of <0.5 nm root mean square (rms). The PE processing introduces topographical features, arising from the Ti mask fabrication and the PE itself. During the former, the samples have been slightly over-etched in the chlorinated RIE in order to ensure full opening of the windows for PE in the Ti masking layer, and this results in regular trenches of width w_{RIE}. Furthermore, the introduction of protons into LN induces significant lattice distortions, which on *z*-cut substrates, results in a swelling of the crystal surface.[33,34] Accordingly, the PE regions can be identified in the atomic force microscopy (AFM) topography images (Figures 2a and 3a) as swollen areas of width w_{PE} at the crystal surface, containing an eroded region of width w_{RIE}. The periodicity (~6 μm) of the PE areas is in agreement with the mask dimensions. Despite the etching-induced damage, the average surface roughness of the PPELN surfaces is 2 nm rms. The RIE trench depth is spatially inhomogeneous. In some instances, particularly on the $+z$ crystal surface, the PE_{RIE} region is even slightly raised due to the PE-induced swelling.

The electrostatic properties of the PPELN surfaces have been characterized using electrostatic force microscopy (EFM). The EFM phase image (Figure 2c) of the $-z$ surface has been acquired simultaneously (in lift mode) with the topography image shown in Figure 2a. The locations where the electrostatic signal changes most abruptly are at the PE−LN interface and within the PE region at the PE_{LD}−PE_{RIE} interface. This correlates well with the electric field modeling (Figure 1), which shows a difference in the out-of-plane field component between PE and LN regions and a strong in-plane field component at the PE−LN boundary. There is a strong correlation between the surface topography and the EFM phase images, as shown in the line profile cross sections of the topography and EFM phase images (Figure 2b,d, respectively). Given the large tip−sample electrostatic forces present and the small lift height, it is likely that the tip interacts mechanically with the surface; however, this is not expected to affect the qualitative observations of the field gradient at the boundary between PE and LN regions. The topography and EFM phase images (Figure 3a,c) of the $+z$ surface

and their line profiles (Figure 3b,d) show a similar behavior to the $-z$ PPELN surface.

In order to determine the effect of PE on the piezoelectric properties of proton-exchanged LN, piezoresponse force microscopy (PFM) has been used.[35] PFM amplitude images (Figures 2e and 3e from different locations than Figures 2a−d and 3a−d), illustrate a reduction of the piezoelectric response from PE regions. To correlate the PFM with the topography and EFM images, line profiles (Figures 2f and 3f) have been indicated. The regions with the highest piezoresponse correspond to the LN crystal, whereas the PE region can be identified from the RIE trench and adjacent swelling and has markedly reduced piezoresponse. The lateral inhomogeneities in the piezoresponse from the PE areas may be a result of a non-uniform diffusion-limited PE process under the mask. The PFM phase images (insets to Figures 2e and 3e) show the expected $+90°$ and $-90°$ signal for $-z$ and $+z$ surfaces, respectively, but also demonstrate that the direction of the polarization is preserved in the PE regions.

The $\pm z$ PPELN crystal surfaces have been imaged using AFM again after exposure to light of 254 nm wavelength for 10 min (Figure 4a,c). There is clear evidence of Ag nanoparticle deposition at the boundary between the PE and LN regions. From the line profiles (Figure 4b,d), the deposited region is determined to be 2.71 ± 0.14 and 2.58 ± 0.11 μm wide and 17.17 ± 0.79 and 15.38 ± 0.66 nm high for the $-z$ and $+z$ surfaces, respectively (in all cases, the reported value is averaged for $n = 10$ measurements). Careful inspection reveals that the Ag has reduced preferentially on the PE side of the LN−PE interface (in the PE_{LD} region) for both crystal surfaces. As control experiments, we have determined that deposition does not occur under the same parameters in visible light or under illumination from a 365 nm pen lamp, nor does deposition occur in regions that have been uniformly proton-exchanged (as judged by the surface roughness of before and after images, which are within 0.3 nm rms of each other). These results demonstrate that both wavelength and electric field are important parameters. Limited deposition does occur in a region of the samples where there is uniform PE and periodic RIE. In this case, Ag nanostructures with heights of 2.5 ± 0.5 and 3.8 ± 1.1 nm form on $-z$ and $+z$ surfaces, respectively, along a topographic feature resulting from the processing ($n = 10$). This highlights the need for further research to determine the effect of RIE damage and etching in hydrofluoric acid, and also suggests that the routes for fabricating LN crystal templates with engineered reactivity are not limited to electric field poling and PE.

DISCUSSION

In previous studies of LN, deposition has occurred on domain walls, which resulted in the formation of

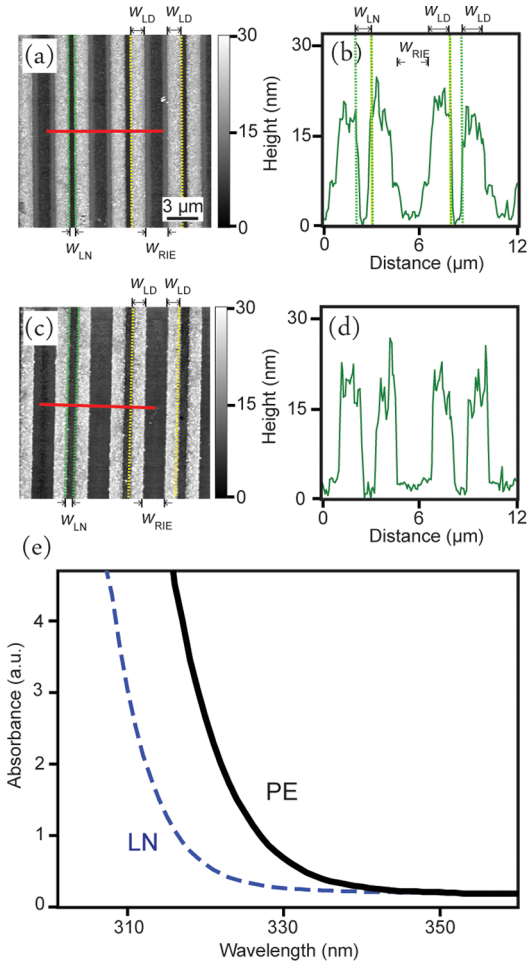

Figure 4. (a,c) AFM topography images and (b,d) corresponding line profiles [location indicated in (a,b)] after photodeposition on the $-z$ and $+z$ PPELN surfaces, respectively. (e) Measured absorbance (log(transmission/100%)) in the UV range for untreated and proton-exchanged LN crystals: blue and black lines, respectively. Spectra have been recorded on 0.5 mm thick congruent samples (transmission along the crystal *c*-axis). The proton-exchanged crystal had PE layers on both surfaces, amounting to a total PE thickness of 2.56 μm.

nanowire-like structures,[19,30] but also on the $+z$ and $-z$ domains depending on the intensity and wavelength of the illumination.[21,22] In the present study, deposition has occurred preferentially in the PE_{LD} regions at the PE−LN interface. These results can be explained by the presence of an electric field, which allows the electrons to participate in the photochemical reduction of Ag^+ to Ag^0. As described before, there is qualitative agreement with the modeling of the electric field components (Figure 1) and the measured electrostatic interactions (Figures 2c and 3c), both of which support the presence of a field at the PE−LN boundary.

At the PE−LN interface, where the magnitude of the in-plane field is at a maximum, the photogenerated electrons are moved from the LN toward the PE−LN interface, resulting in deposition in the PE_{LD} region for the $-z$ surface. For the $+z$ surface, even though the field at the PE−LN interface should push the electrons

toward the LN side of the boundary, the deposition also occurs preferentially in the PE_{LD} region. Thus, the in-plane field alone cannot entirely explain the observed results. The electric field distribution is asymmetric around the PE−LN interface (Figure 1c) owing to the parabolic curvature of the depth of the PE region. This may contribute to the observed preferential deposition on the PE side of the PE−LN interface for both surfaces. Thus, the out-of-plane component of the electric field also plays a role in the deposition behavior. In the center of the LN and PE regions, the in-plane field component is reduced compared to the field at the PE−LN boundary, and the out-of-plane component of the electric field acts to deplete electrons ($-z$) or to keep them at the surface ($+z$). Therefore, the electrons generated in the PE region on the $+z$ surface would accumulate at the surface of the PE_{LD} region and react with the Ag^{+}.

Consideration of the out-of-plane component of the electric field suggests there could be photodeposition in the LN and PE_{RIE} regions on the $+z$ surface, as electrons will be kept at the surface. There is a slight increase in the surface roughness (0.7 to 1.0 nm rms) for the LN region after deposition on the $+z$ surface (visible in Figure 4d), suggesting that some deposition may have occurred there, although comparison of the roughness of LN regions in images taken before and after photodeposition does not always show this. Given the appearance of a well-defined RIE trench in the as-prepared $+z$ surface (Figure 3a), and the apparent partially filled trench after the deposition on the $+z$ surface (Figure 4c), it is possible that some Ag has deposited in the PE_{RIE} region, as well. However, as stated previously, there are inhomogeneities in the as-prepared RIE trench depth, and without performing *in situ* deposition experiments or finding the same location before and after the deposition, it is difficult to determine absolutely whether deposition occurs in the PE_{RIE} region.

While the results obtained are consistent with electrostatic field-directed charge accumulation, the observed behavior could further be explained by differences in the mobility or UV absorption edge in PE and LN regions. Göring *et al.* have shown that the photoconductivity of proton-exchanged LN under illumination with light of 514 nm wavelength is larger than that of LN, which is attributed to an ion migration process.[36] It is therefore reasonable to assume a different conductivity between PE and LN regions. This difference in the electrical properties could influence the photodeposition process on these surfaces. Another possible explanation could be increased absorption and a corresponding higher number of photogenerated charge carriers in the PE regions. A comparison between the UV absorption edge measured in untreated LN and planar proton-exchanged LN crystals (with a Cary500 spectrophotometer) supports such an hypothesis, by providing evidence for a slight shift to longer wavelengths of the UV edge in proton-exchanged LN (Figure 4e). Our results indicate that, in addition to the electric field distribution at the surface, the optoelectronic properties such as photoconductivity or a shift in the absorption edge play an important role in the photochemical reactivity of PPELN surfaces. Further studies are necessary to fully understand this interplay.

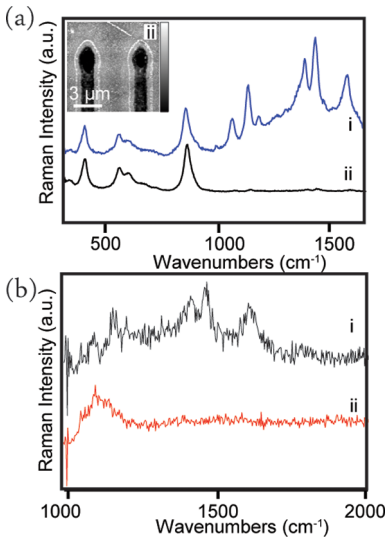

Figure 5. (a) SERS signal from the substrate and the probe molecule 4-aminothiophenol adsorbed onto the Ag nanostructures formed on the surface of (i) the periodically proton-exchanged area (Figure 4a) and (ii) the region that has been uniformly proton-exchanged with periodic RIE stripes (AFM topography image is shown as an inset to (a)). (b) (i) SERS signal from the same region as a(ii), and (ii) signal from 4-aminothiophenol and LN for a sample exposed to the 4-aminothiophenol/methanol solution after the nanostructures have been removed (for wavenumbers greater than 1000). The *z*-data scale for the inset in (a) is 10 nm.

To demonstrate the functionality of these photodeposited metallic nanostructures, the $-z$ crystal has been immersed in a SERS-active 4-aminothiophenol/methanol solution. Plasmons can be excited on silver nanostructures when light creates a collective oscillation of the conduction electrons on the surface of the metal.[37−39] Figure 5a shows SERS of the target molecule, 4-aminothiophenol, which was assembled onto the Ag nanostructure array. Only Raman bands below $\sim$1000 cm^{-1} can be accounted for by LN.[40] Figure 5a(i) shows the Raman spectra for the PPELN region of the sample, which contains nanostructures similar to the ones shown in Figure 4. The Raman spectral features above $\sim$1000 cm^{-1} possess several intense bands, which can be assigned to 4-aminothiophenol.[41] The band positions and relative intensities of these bands are in agreement with the spectral features for SERS from 4-aminothiophenol, which arise from a combination of a- and b-type vibrational symmetries.[41] In Figure 5a(ii), the intensity of the signal is reduced significantly. This Raman spectrum corresponds to the region that has been uniformly proton-exchanged but retains some topography associated with the RIE process, which

contributed to the deposition of a thin Ag nanostructure (inset to Figure 5a).

Figure 5b(i) shows the Raman spectrum above ~1000 cm^{-1} recorded for the probe molecule 4-aminothiophenol absorbed onto the substrate in the same region. Weak spectral features above ~1000 cm^{-1} can be seen, demonstrating that SERS can be observed from arrays of 2−3 nm high nanostructures. The band positions and relative intensities enable assignment of the Raman bands to the probe molecule. Figure 5b(ii) shows the Raman spectra for the substrate with the probe molecule only (the metallic structures were removed from the surface, and the sample was exposed to the probe molecule as before). No probe molecule can be seen in the Raman signal. Overall, the Raman spectra in Figure 5 indicate that the Ag nanostructures support plasmon-assisted Raman (*i.e.*, SERS). Such SERS-active nanostructures may be of interest for applications that require precise control over nanostructure size, shape, and distribution.

CONCLUSION

To summarize, we have used a chemical patterning technique to periodically pattern the optical, piezoelectric, and ferroelectric properties of a LN crystal. We have used these modulated properties to drive the assembly of metallic nanostructures, which have been further shown to be SERS-active. The deposition of Ag is dictated primarily by the lateral component of the electric field at the surface, which is strongest at the interface between LN and PE regions, and largely confined to the PE_{LD} region formed when protons diffused under the Ti mask used to fabricate the PPELN templates. Whereas nanowires formed on periodically poled LN are limited to the domain wall width and the geometry of the domain, on PPELN, the width of the PE region, and hence the nanostructure width, can be controlled *via* processing conditions. We show that, under the experimental conditions normally used to obtain nanowires along domain walls on periodically poled LN, it is possible to obtain wider nanostructures using chemical patterning. PE and photodeposition thus provide a way to control both the properties of the LN and the width of the deposited nanostructures. Ag deposition and SERS have also been observed from PE regions patterned *via* RIE, demonstrating the feasibility of alternative patterning routes. Notably, patterning by PE may enable new ways to fabricate complex nanostructures and control local reactivity from nano- to microscales for a range of sensing applications. Additionally, PE provides a route for combining the nonlinear optical properties of the substrates with the nanostructures formed at the surface for novel applications.

MATERIALS AND METHODS

Fabrication. We used 1.6 × 1.6 cm^2 samples, diced from optical grade, *z*-cut, 0.5 mm thick, 3 in. congruent LN wafers (CasTech Inc.). In order to selectively proton exchange the samples, a 100 nm thick Ti mask was patterned onto either the $-z$ or $+z$ crystal surfaces using standard photolithography and RIE in a Cl_2/Ar atmosphere. The Ti mask consisted of periodic stripes, parallel to the *y*-axis of the substrate (period along *x*: Λ = 6.09 μm). PE was then performed through the Ti mask openings (w_{RIE}) by immersing the samples for 24 h in benzoic acid at 200 °C. On the basis of calibrations using a prism coupling method,[42] these processing conditions correspond to a PE depth of ~2.7 μm. The lateral diffusion of protons under the Ti stripes[25,26] resulted in final PE widths which were broader than the original mask openings. After the PE processing, the Ti layer was removed by etching in a hydrofluoric acid solution for ~4 s, leaving a patterned PPELN crystal with LN and PE regions, as illustrated in Figure 1a. The parabolic shape of the PE region, visible in the schematic of the cross section (Figure 1a), is a consequence of the PE diffusion proceeding in depth (*z*) as well as in the lateral direction underneath the Ti mask (*x*).

The PE−LN boundary corresponds to the sharp transition between a region where ferroelectric properties are significantly reduced[25,26,43] by the substitution of Li^+ with H^+ and the substrate, characterized by a spontaneous polarization, P_{SLN} ~ 75 $\mu C/cm^2$.[44] Accordingly, the strong gradient of P_s gives rise to embedded electric fields, localized at the PE−LN interfaces. The resulting electric fields have been modeled using COMSOL Multiphysics.

Photodeposition. Prior to the photodeposition experiments, the samples were cleaned *via* sonication for 20 min each in isopropyl alcohol, acetone, and pure water (Milli-Q water, 18.3 MΩcm). The crystal was placed on a glass slide, and 150 μL of 0.01 M $AgNO_3$ solution was pipetted onto the surface. The samples were then illuminated for 10 min each with a super-band-gap light source (Spectroline 254 nm wavelength pen lamp) at a distance of 2 cm above the surface (with specified power density, 2000 $\mu W/cm^2$). As a control, the samples were also illuminated under the same conditions with a sub-band-gap light source (Spectroline 365 nm wavelength pen lamp with a specified power density of 1000 $\mu W/cm^2$) and with visible light. After illumination, the samples were immersed in pure water for 1 min and then blown dry with nitrogen.

AFM. AFM measurements were performed with a MFP-3D atomic force microscope (Asylum Research) equipped with highly doped PPP-NCH cantilevers (Nanosensors) having nominal resonant frequencies of 330 kHz and spring constants of 42 N/m. Prior to the AFM experiments, the tips were cleaned with ethanol and exposed to UV (BioForce UV/Ozone ProCleaner) for 10 min. AFM was used to image the surface topography and the piezoelectric and electrostatic properties of the substrates. Prior to, and after the deposition, the samples were imaged using amplitude modulation mode. To remove the deposited Ag, the samples were cleaned using the protocol mentioned above; however, between the isopropyl alcohol and acetone sonication steps, the samples were gently rubbed with lens tissue soaked in isopropyl alcohol. During the sonication to remove the deposited silver, the nanoparticles can be harvested from the surface. After cleaning, the samples were imaged again to ensure the deposited Ag had been completely removed from the surfaces in order to reuse the samples.

EFM and PFM. The electrostatic and piezoelectric properties of the samples were obtained using EFM and PFM, respectively.[45,46] EFM images were recorded in lift mode on the MFP-3D, whereby the tip is raised by a defined lift height above the surface after recording the topography on a complete scanline. The tip then follows the contour line of the

topography from the previous scanline at the given lift height. At the same time, the mechanical excitation is switched off. Instead, an AC voltage at the resonance frequency of the cantilever is applied between tip and sample. The electrostatic interaction with the surface induces a mechanical vibration in the cantilever that can be correlated to the local electric field present underneath the tip. In our experiment, the lift height was 10 nm and the AC voltage was 1 V.

During PFM, a 5 V AC voltage (600 kHz) was applied to the highly doped PPP-NCH tip during contact mode imaging, resulting in surface deformations *via* the converse piezoelectric effect. These surface deformations were recorded by monitoring the tip deflection and demodulated into amplitude and phase signals using a HF2LI (Zurich Instruments) lock-in amplifier. The topography was recorded simultaneously with the PFM signals *via* the MFP-3D controller. The PFM amplitude image provides information on the magnitude of the bias-induced deformation of the sample, and the PFM phase image provides information on the orientation of the spontaneous polarization. By convention, a phase offset is chosen such that a $-z$ domain will exhibit a $+90°$ PFM phase signal and a $+z$ domain will exhibit a $-90°$ signal. Thus, PFM phase images of LN crystals will have $+90°$ and $-90°$ signal for $-z$ and $+z$ surfaces, respectively.

SERS. For SERS measurements, a monolayer of 4-aminothiophenol was prepared by immersing the sample (after a photodeposition experiment) in 2 mM 4-aminothiophenol/methanol solution for 15 min. The sample was then dipped in methanol for 5 min to rinse off any excess molecules, and left to dry. The 4-aminothiophenol monolayer was excited at 532 nm. The laser was linearly polarized at a 45° angle relative to the laboratory *y*-axis with the direction of the laser along the *z*-axis. The sample was placed so that the nanostructures were orientated along the *x*-axis. The Raman signal was collected at a backscattered angle and directed onto a charge-coupled device *via* a monochromator.

Conflict of Interest: The authors declare no competing financial interest.

Acknowledgment. This publication has emanated from research conducted with the financial support of the Higher Education Authority PRTLI-5 (DGPP and NANOREMEDIES), Science Foundation Ireland (SFI10/RFP/MTR2855), and UCD Research. This work was also supported by the Swedish Scientific Research Council (VR 622-2010-526 and 621-2011-4040) and the ADOPT Linné Center. The authors are grateful to COST actions MP0702 (STSM 8171) and MP0904 and the Rank Prize Mini-Symposium on Periodically-Modulated and Artificially Hetero-Structured Devices (2009), which facilitated the work, and to J.I. Kilpatrick for technical assistance. S.A.L.W. also acknowledges support from the Alexander von Humboldt Foundation, and K.G. is grateful for the support of the European Commission through a Marie Curie Fellowship (PIEF-2009-234798).

REFERENCES AND NOTES

1. Kalinin, S. V.; Bonnell, D. A.; Alvarez, T.; Lei, X.; Ferris, J. H.; Zang, Q.; Dunn, S. Atomic Polarization and Local Reactivity on Ferroelectric Surfaces: A New Route toward Complex Nanostructures. *Nano Lett.* **2002**, *2*, 589–593.
2. Kalinin, S. V.; Bonnell, D. A.; Alvarez, T.; Lei, X.; Hu, Z.; Shao, R.; Ferris, J. H. Ferroelectric Lithography of Multicomponent Nanostructures. *Adv. Mater.* **2004**, *16*, 795–799.
3. Zhang, Z.; Sharma, P.; Borca, C. N.; Dowben, P. A.; Gruverman, A. Polarization-Specific Adsorption of Organic Molecules on Ferroelectric $LiNbO_3$ Surfaces. *Appl. Phys. Lett.* **2010**, *97*, 243702.
4. Zhang, Z.; González, R.; Díaz, G.; Rosa, L. G.; Ketsman, I.; Zhang, X.; Sharma, P.; Gruverman, A.; Dowben, P. A. Polarization Mediated Chemistry on Ferroelectric Polymer Surfaces. *J. Phys. Chem. C.* **2011**, *115*, 13041–13046.
5. Li, D.; Zhao, M. H.; Garra, J.; Kolpak, A. M.; Rappe, A. M.; Bonnell, D. A.; Vohs, J. M. Direct *In Situ* Determination of the Polarization Dependence of Physisorption on Ferroelectric Surfaces. *Nat. Mater.* **2008**, *7*, 473–477.
6. Garra, J.; Vohs, J. M.; Bonnell, D. A. The Effect of Ferroelectric Polarization on the Interaction of Water and Methanol with the Surface of $LiNbO_3$. *Surf. Sci.* **2009**, *603*, 1106–1114.
7. Ehre, D.; Lavert, E.; Lahav, M.; Lubomirshy, I. Water Freezes Differently on Positively and Negatively Charged Surfaces of Pyroelectric Materials. *Science* **2010**, *327*, 672–675.
8. Stock, M.; Dunn, S. $LiNbO_3$-A New Material for Artificial Photosynthesis. *IEEE Trans.* **2011**, *58*, 1988–1993.
9. Giocondi, J. L.; Rohrer, G. S. Spatially Selective Photochemical Reduction of Silver on the Surface of Ferroelectric Barium Titanate. *Chem. Mater.* **2001**, *13*, 241–242.
10. Giocondi, J. L.; Rohrer, G. S. Spatial Separation of Photochemical Oxidation and Reduction Reactions on the Surface of Ferroelectric $BaTiO_3$. *J. Phys. Chem. B* **2001**, *105*, 8275–8277.
11. Jones, P.; Dunn, S. Photo-reduction of Silver Salts on Highly Heterogeneous Lead Zirconate Titanate. *Nanotechnology* **2007**, *18*, 185702.
12. Jones, P.; Gallardo, D. E.; Dunn, S. Photochemical Investigation of a Polarizable Semiconductor, Lead-Zirconate-Titanate. *Chem. Mater.* **2008**, *20*, 5901–5906.
13. Jones, P. M.; Dunn, S. Interaction of Stern Layer and Domain Structure on Photochemistry of Lead-Zirconate-Titanate. *J. Phys. D: Appl. Phys.* **2009**, *42*, 065408.
14. Dunn, S.; Sharp, S.; Burgess, S. The Photochemical Growth of Silver Nanoparticles on Semiconductor Surfaces-Initial Nucleation Stage. *Nanotechnology* **2009**, *20*, 115604.
15. Dunn, S.; Jones, P. M.; Gallardo, D. E. Photochemical Growth of Silver Nanoparticles on C− and C+ Domains on Lead Zirconate Titanate Thin Films. *J. Am. Chem. Soc.* **2007**, *129*, 8724–8728.
16. Liu, X. Y.; Kitamura, K.; Terabe, K.; Hatano, H.; Ohashi, N. Photocatalytic Nanoparticle Deposition on $LiNbO_3$ Nanodomain Patterns via Photovoltaic Effect. *Appl. Phys. Lett.* **2007**, *91*, 044101.
17. Liu, X. Y.; Ohuchi, F.; Kitamura, K. Patterning of Surface Electronic Properties and Selective Silver Deposition on $LiNbO_3$. *Funct. Mater. Lett.* **2008**, *1*, 177–182.
18. Dunn, S.; Tiwari, D. Influence of Ferroelectricity on the Photoelectric Effect of $LiNbO_3$. *Appl. Phys. Lett.* **2008**, *93*, 092905.
19. Hanson, J. N.; Rodriguez, B. J.; Nemanich, R. J.; Gruverman, A. Fabrication of Metallic Nanowires on a Ferroelectric Template via Photochemical Reaction. *Nanotechnology* **2006**, *17*, 4946–4949.
20. Prokhorov, A. M.; Kuzminov, Y. S. *Physics and Chemistry of Crystalline Lithium Niobate*; Taylor & Francis: New York, 1990.
21. Sun, Y.; Nemanich, R. J. Photoinduced Ag Deposition on Periodically Poled Lithium Niobate Wavelength and Polarization Screening Dependence. *J. Appl. Phys.* **2011**, *109*, 104302.
22. Sun, Y.; Eller, B. S.; Nemanich, R. J. Photo-induced Ag Deposition on Periodically Poled Lithium Niobate Concentration and Intensity Dependence. *J. Appl. Phys.* **2011**, *110*, 084303.
23. Yamada, M.; Nada, N.; Saitoh, M.; Watanabe, K. First-Order Quasi-Phase Matched $LiNbO_3$ Waveguide. *Appl. Phys. Lett.* **1993**, *62*, 435–436.
24. Jackel, J. L.; Rice, C. E.; Veselka, J. L. Proton Exchange for High-Index Waveguides in $LiNbO_3$. *Appl. Phys. Lett.* **1982**, *41*, 607–609.
25. Manzo, M.; Laurell, F.; Pasiskevicius, V.; Gallo, K. Two-Dimensional Domain Engineering in $LiNbO_3$ via a Hybrid Patterning Technique. *Opt. Mater. Express* **2011**, *1*, 365–371.
26. Manzo, M.; Laurell, F.; Pasiskevicius, V.; Gallo, K. Electrostatic Control of the Domain Switching Dynamics in Congruent $LiNbO_3$ via Periodic Proton-Exchange. *Appl. Phys. Lett.* **2011**, *98*, 122910.
27. Wilson, R. G.; Novak, S. W.; Zavada, J. M.; Loni, A.; De La Rue, R. M. Secondary Ion Mass Spectrometry Depth Profiling of Proton-Exchanged $LiNbO_3$ Waveguides. *J. Appl. Phys.* **1989**, *66*, 6055.

28. Korkishko, Yu. N.; Fedorov, V. A. *Ion Exchange in Single Crystals for Integrated Optics and Optoelectronics*; Cambridge International Science Publisher: Cambridge, 1999; pp 127−143.
29. Schröder, S.; Haussmann, A.; Thiessen, A.; Soergel, E.; Woike, T.; Eng, L. M. Conducting Domain Walls in Lithium Niobate Single Crystals. *Adv. Mater.* **2012**, DOI: 10.1002/adfm.201201174.
30. Haussmann, A.; Milde, P.; Erler, C.; Eng, L. M. Ferroelectric Lithography Bottom-Up Assembly and Electrical Performance of a Single Metallic Nanowire. *Nano Lett.* **2009**, *9*, 763–768.
31. Zheng, G.; Patolsky, F.; Cui, Y.; Wang, W. U.; Lieber, C. M. Multiplexed Electrical Detection of Cancer Markers with Nanowire Sensor Arrays. *Nat. Biotechnol.* **2005**, *23*, 1294–1301.
32. Lal, S.; Link, S.; Halas, N. J. Nano-Optics from Sensing to Waveguiding. *Nat. Photonics* **2007**, *1*, 641–648.
33. Zhou, F.; Matteo, A. M.; De La Rue, R. M.; Ironside, C. N. Swelling Characteristics of Proton-Exchanged $LiNbO_3$ Waveguides. *Electron. Lett.* **1992**, *28*, 87–89.
34. de Souza, R. E.; Engelsberg, M.; Pacobahyba, L. H.; do Nascimento, G. C. Nuclear Magnetic Resonance Study of Proton Exchanged $LiNbO_3$. *J. Appl. Phys.* **1995**, *77*, 408.
35. Manzo, M.; Denning, D.; Rodriguez, B. J.; Gallo, K. Piezoresponse Force Microscopy on Proton Exchanged $LiNbO_3$ Layers. In *Lasers, Sources, and Related Photonic Devices*; OSA Technical Digest (CD) (Optical Society of America, 2012), paper IF1A.5.
36. Göring, R.; Yuan-Ling, Z.; Steinberg, S. Photoconductivity and Photovoltaic Behaviour of $LiNbO_3$ and $LiNbO_3$ Waveguides at High Optical Intensities. *Appl. Phys. A: Mater. Sci. Process.* **1992**, *55*, 97–100.
37. Lordan, F.; Rice, J. H.; Jose, B.; Forster, R. J.; Keyes, T. E. Surface Enhanced Resonance Raman and Luminescence on Plasmon Active Nanostructured Cavities. *Appl. Phys. Lett.* **2010**, *97*, 153110.
38. Lordan, F.; Rice, J. H.; Jose, B.; Forster, R. J.; Keyes, T. E. Site Selective Surface Enhanced Raman on Nanostructured Cavities. *Appl. Phys. Lett.* **2011**, *99*, 033104.
39. Lordan, F.; Rice, J. H.; Jose, B.; Forster, R. J.; Keyes, T. E. Effect of Cavity Architecture on the Surface-Enhanced Emission from Site-Selective Nanostructured Cavity Arrays. *J. Phys. Chem. C* **2012**, *116*, 1784–1788.
40. Schaufele, R. F.; Weber, M. J. Raman Scattering by Lithium Niobate. *Phys. Rev.* **1966**, *152*, 705–708.
41. Wu, D.; Liu, X.; Huang, Y.; Ren, B.; Xu, X.; Tian, Z. Surface Catalytic Coupling Reaction of *p*-Mercaptoaniline Linking to Silver Nanostructures Responsible for Abnormal SERS Enhancement: A DFT Study. *J. Phys. Chem. C* **2009**, *113*, 18212–18222.
42. Tien, P. K.; Ulrich, R. Theory of Prism-Film Coupler and Thin-Film Light Guides. *J. Opt. Soc. Am.* **1970**, *60*, 1325–1337.
43. Korkishko, Yu.N.; Fedorov, V. A.; Laurell, F. *IEEE J. Quantum Electron.* **2000**, *6*, 1.
44. Myers, L. E.; Eckardt, R. C.; Fejer, M. M.; Byer, R. L.; Bosenberg, W. R.; Pierce, J. W. Quasi-Phase-Matched Optical Parametric Oscillators in Bulk Periodically Poled $LiNbO_3$. *J. Opt. Soc. Am. B* **1995**, *12*, 2102–2116.
45. Saurenbach, F.; Terris, B. D. Imaging of Ferroelectric Domain-Walls by Force Microscopy. *Appl. Phys. Lett.* **1990**, *56*, 1703–1705.
46. Rodriguez, B. J.; Nemanich, R. J.; Kingon, A.; Gruverman, A.; Kalinin, S. V.; Terabe, K.; Liu, X.; Kitamura, K. Domain Growth Kinetics in Lithium Niobate Single Crystals Studied by Piezoresponse Force Microscopy. *Appl. Phys. Lett.* **2005**, *86*, 012906.